Article

Effect of Infill Parameters and Nano-Reinforcement on Compression Performance of 3D Printed Polylactic Acid

Dorivane Farias , Dhonata Caldas Oliveira , Luciano Quaresma , Mário Sousa , Miriane Alexandrino Pinheiro , Rômulo S. Angélica , Simone Patrícia Aranha Da Paz , Marcos Allan Leite Dos Reis *

Posted Date: 5 February 2024

doi: 10.20944/preprints202402.0299.v1

Keywords: Infill Patterns; Fused Deposition Modeling; Mechanical Properties; Nanocomposite.

Article

Effect of Infill Parameters and Nano-Reinforcement on Compression Performance of 3D Printed Polylactic Acid

Dorivane Farias [1,2], Dhonata Oliveira [1,2], Luciano Quaresma [1,2], Mário Sousa [2], Miriane Pinheiro [3], Romulo Angélica [4], Simone Paz [4] and Marcos Reis [1,2,3,*]

[1] Materials Science and Engineering Program, Federal University of Para, Ananindeua, PA, Brazil
[2] Laboratory of 3D Nanostructuring, Federal University of Para, Belem, PA, Brazil
[3] Engineering of Natural Resources of the Amazon Program, Federal University of Para, Belem, PA, Brazil
[4] Graduate Program in Geology and Geochemistry, Federal University of Para, Belem, PA, Brazil
[*] Correspondence: marcosallan@ufpa.br

Abstract: With the advancement of Additive Manufacturing and its applications in various industrial segments, it becomes increasingly important to investigate the processability parameters associated with nano-reinforcement. This study examines the influence of infill parameters, such as patterns (hexagonal, triangular and concentric), shape (solid and honeycomb) and concentrations by mass of Carbon Nanotubes (CNTs) at 1.0 wt% and 2.0 wt% on the mechanical compression properties of the 3D printed material. In this sense, nanocomposites based on Polylactic Acid (PLA) matrix nano-reinforced by CNTs were characterized using the Scanning Electron Microscopy -SEM, X-ray Diffraction, Raman Spectroscopy techniques and mechanical analysis. The mechanical properties of both the matrix and the nanocomposites were determined through mechanical compression tests, in accordance with [1]. SEM revealed compacted regions, voids, and detachment in the structures. XRD characterization indicated PLA predominantly amorphous nature, while CNTs exhibited characteristic diffractions of carbon nanotubes. Raman characterization showcased bands and characteristic vibrations of CNTs and PLA, nanocomposites' vibrational modes combine those of CNTs and PLA. Mechanical compression analysis indicates a direct influence of infill pattern, shape, and nano-reinforcement. The triangle pattern outperformed other patterns, exhibiting a 15.03% increase compared to concentric and 8.8% compared to hexagon infill. In nanocomposites, all showed higher compressive strength than the matrix. For PLA/1.0%CNTs, strength was 16.8%, and for PLA/2.0%CNTs, it reached 39.2%. In honeycomb shapes with infill variations, the triangular pattern excelled with a 0.97% increase over concentric and 6.12% over hexagon patterns. Honeycomb results indicate a 59.6% increase for (PLA/1.0%CNTs) and a 0.48% increase for (PLA/2.0%CNTs) compared to the matrix. This study highlights 3D printing parameters, emphasizing the effectiveness of the triangular pattern and the enhanced strength with the addition of CNTs, providing insights to enhance products manufactured through Additive Manufacturing.

Keywords: infill patterns; fused deposition modeling; mechanical properties; nanocomposite

1. Introduction

3D printing innovates in the manufacturing of new materials and expands options for existing ones [2]. Polymeric materials in 3D printing generate lightweight and intricate structures, valuable in sectors such as aerospace, medicine (tissues, organs), and various other fields [3]. Several 3D printing methods exist, with Fused Deposition Modeling (FDM) being notable for its simplicity and cost-effectiveness, contributing to its widespread adoption [4]. In this technique, the filament is heated until melted and then extruded by the machine (3D printer). The nozzle moves in three directions to deposit the polymer on the build plate, following the instructions of the *G-Code*. The filament is continuously fed by the extruder and nozzle, while the material is deposited on the plate until it achieves the desired shape [5]. Polymers like PLA, ABS, Nylon, ASA, and PET are common in FDM, and various reinforcement options such as CNTs, graphene, copper, iron fillers, carbon fibers (continuous and short), glass, and Kevlar can be integrated [6].

The infill pattern impacts the mechanical properties of the piece and determines how filled filaments interact under loading [7]. The addition of nanomaterials has been employed as nanofillers to enhance the performance of polymers [8].

The main advantages of nanoscale materials lie in their large surface area, resulting in a significant interfacial volumetric fraction of material [9]. In nanocomposites, nanoscale dimensions create crucial interfaces for property enhancement [10]. Nanocomposites feature a matrix as the major constituent and reinforcing agents that improve properties [11]. Nanocomposite materials are categorized into three groups based on the composing matrix: ceramic, polymeric, and metallic [10]. The incorporation of MWCNTs into widely used thermoplastic polymers can enhance their mechanical properties [12]. Notably, in nanocomposites with polymeric matrices, the addition of carbon nanotubes increases plastic deformation, consequently improving material fracture toughness [13].

Polymeric nanocomposites are advanced classes of materials that exhibit superior performance due to the beneficial interaction between the polymer (matrix) and nano materials (reinforcements) [14]. However, interfacial interaction/bonding, material composition and structural defects need to be analyzed in detail to ensure excellent product performance [15]. In this class of materials, characterization is crucial for understanding their basic properties, whether chemical or physical. Several techniques have been used in the characterization of nanocomposites, these techniques include Optical Microscopy, Scanning Electron Microscopy, High Transmission Electron Microscopy, Raman Spectroscopy, Atomic Force Microscopy and X-ray Diffraction, as these have proven to be very useful for quantifying nanocomposites [16].

The exceptional characteristics of carbon nanotubes make them an ideal reinforcement for a variety of materials, including polymers, metals/alloys, and ceramics. Nanotube-based composites are considered an alternative to smart materials [17]. Furthermore, the addition of CNTs to a PLA matrix, for instance, can facilitate the crystallization process of PLA and enhance the degree of crystallinity [18]. The unique properties of CNTs are believed to have ushered in a new era in the materials world, especially in the field of conductive polymers and CNT-based nanocomposites [19].

PLA is derived through the polymerization of lactic acid, which is sourced from renewable and abundant materials like corn and cassava. The lactic acid production process is pollution-free, and the resulting product can biodegrade for circulation in nature, making it an ideal green polymeric material [20]. PLA offers good processability and mechanical properties, durability, and transparency compared to other biodegradable polymers. It is widely used in short-lived packaging products such as food packaging and disposable items [21]. PLA filament is a cost-effective choice for rapid prototyping, and in the automotive industry, PLA filaments have been employed for 3D-printed tools, jigs, and accessories. 3D-printed PLA parts used in real-world applications must be durable and exhibit good strength [22].

In this way, compression specimens were 3D printed by FDM technique to analyze the effect of infill parameters and nano-reinforcement on mechanical behavior under compression test.

2. Materials and Methods

2.1. Materials

The material used as the matrix phase in the present study was Polylactic Acid (PLA), and as reinforcing agents, Multi-Walled Carbon Nanotubes functionalized with COOH (MWCNTs-COOH). The PLA filaments used were purchased from the company 3D FILA and had the following specifications: diameter of 1.75 mm, printing temperature of 180-230 °C, table temperature of 25-60 °C and white color. The Carbon Nanotubes used were purchased from the company Nanoview Nanotecnologia and had the following configurations: external diameter of 10 -30 nm, 1-10 μm length and purity >95%. The PLA filament went through a fragmentation process into reduced dimensions, followed by the incorporation of MWCNTs-COOH. After that, the mixing materials was extruded under 157° C to obtain the nanocomposite with 1.0 wt% and 2.0 wt% for CNTs.

2.2. Modeling, Slicing and Printing Stage

The samples for the compression test were modeled in two shape: solid and honeycomb, as can be seen in Figure 1. The honeycomb shape followed the dimensions defined by [23].

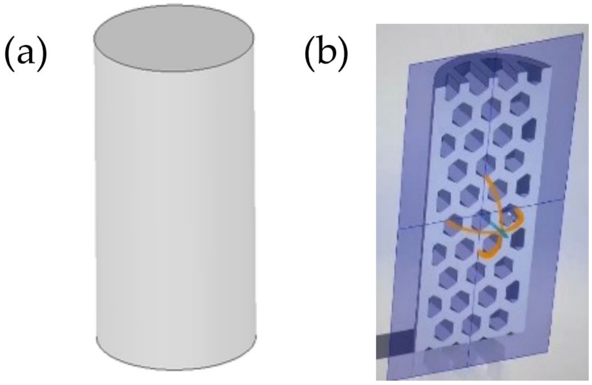

Figure 1. Shape: (a) solid and (b) honeycomb.

At this stage, the following specifications were adopted: printer nozzle diameter of 0.2 mm, filling percentage/density of 90% and infill pattern. In total, three patterns were investigated: concentric, hexagonal and triangular, as can be seen in Figure 2.

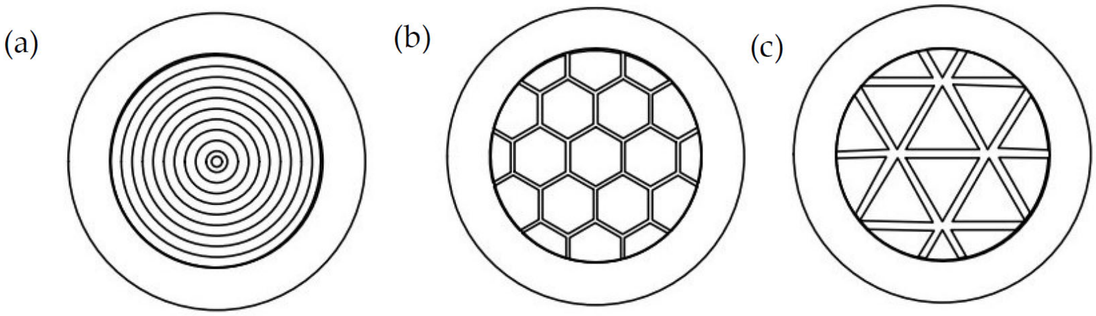

Figure 2. Infill patterns: (a) concentric, (b) honeycomb, (c) triangles.

After slicing, the files were transformed into the *G-Code* version. And, inserted into 3D printers, model Stella 3 Lite, to begin the production stage. Figure 3 shows in detail the FDM process used in the 3D printing.

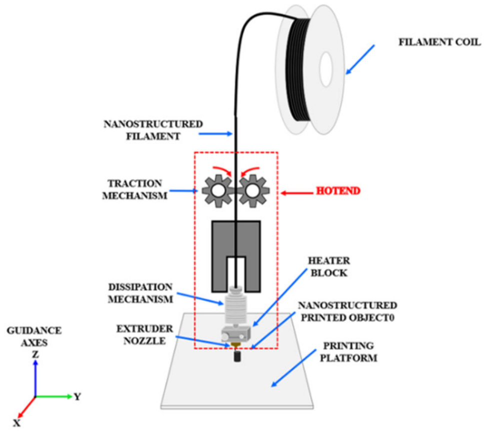

Figure 3. Schematic of FDM process to obtain samples of PLA and PL/CNTs.

2.3. Morphological Characterization by SEM

Morphological analysis was performed on the samples before and after mechanical characterization. The samples were metallized in Au and analyzed using a Scanning Electron Microscope-SEM, TESCAN brand, model MIRA3. Morphological characterizations were carried out with the equipment operating in Secondary Electron detection mode – SE, at an acceleration voltage of 5.0 kV.

2.4. Characterization by X-Ray Diffraction

Characterization by X-ray Diffraction was carried out on samples without the addition of Carbon Nanotubes, on CNTs and on nanocomposites. The analysis was carried out on a PaNalytical diffractometer, using ceramic X-ray tubes with a Co anode ($k\alpha 1$=1.78901 Å).

2.5. Vibrational Characterization by Raman Spectroscopy

Vibrational characterization was performed using a HORIBA Spectrometer, model LabRAM HR EVOLUTION. The characterization was carried out at room temperature, with 514 nm and 633 nm laser line, 20 x lens, accumulation time of 90 s in 5 accumulations, with a power that reaches the sample of 1.44 mW in the spectral region of 40-3800 cm^{-1}.

2.6. Compression Test

The specimens for the compression tests were modeled following the specifications of standard [1]. Six specimens were manufactured for each series. They adopted the shape of a straight cylinder (diameter: 12.7 mm, length: 25.4 mm). A universal testing machine from INTERMETRIC, model iM, equipped with a data acquisition system, a 50 kN load cell, and a standard test speed of 1.3 ± 0.3 mm/min, was employed. Figure 4 illustrates the stages of mechanical compression analysis.

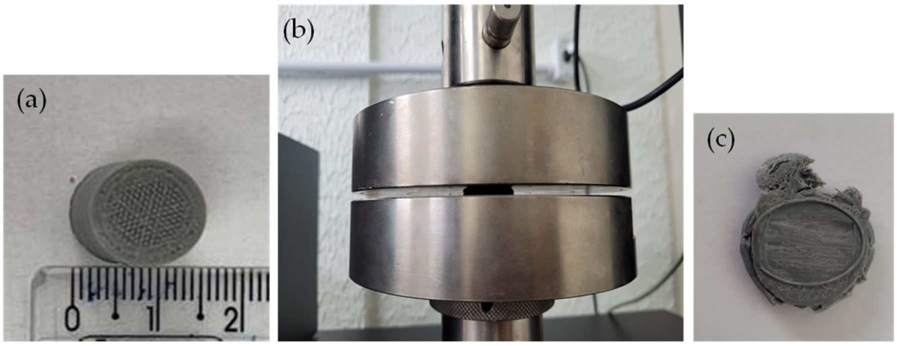

Figure 4. Stages of mechanical compression analyses: (a) the printed specimens, (b) during, and (c) after the mechanical compression test.

For the PLA (matrix) samples, the investigation encompassed the analysis of parameters such as shape (solid and honeycomb) and infill patterns (concentric, hexagons, and triangular). However, for the nanostructured material, infill patterns that exhibited superior performance in each specific type of test were considered. Figure 5 illustrates a flowchart depicting the steps adopted in the fabrication of samples intended for mechanical analyses.

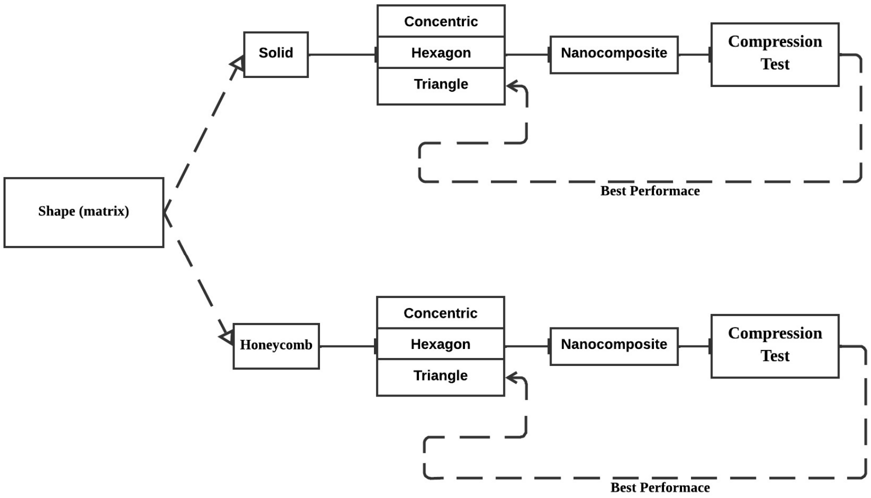

Figure 5. Flowchart of the steps adopted for the fabrication of the materials.

3. Results and Discussion

3.1. Scanning Electron Microscopy Analysis - SEM

The PLA filaments were characterized before and after the incorporation of Carbon Nanotubes through Scanning Electron Microscopy (SEM), and the results are presented in Figure 6.

In Figure 6 (a), the micrograph of the PLA surface prior to the incorporation of MWCNTs-COOH is presented. Upon analyzing the micrograph, the presence of PLA clusters (blue arrows) distributed throughout the surface is evident. Additionally, the existence of a pore (yellow arrow) permeating the material surface is identified. Furthermore, aligned PLA structures (red arrows) are observed, suggesting that PLA can form a microstructure with orientation through the extrusion process [24].

In Figure 6 (b), the morphology of PLA after the incorporation of 1.0 wt% Carbon Nanotubes is depicted. The notable presence of a Carbon Nanotube (yellow arrow) is emphasized, suggesting that CNTs may be dispersed in the PLA matrix through the extrusion method [24]. The occurrence of crack phenomena (red arrows) deserves attention, as they manifest across the entire surface. These cracks, possibly resulting from the initiation of material decomposition during SEM analysis, can be attributed to the sample's fragility under laser incidence. During this analysis, the Scanning Electron

Microscope produces images by moving a focused beam of electrons across the sample's surface while scanning, allowing for a more detailed study of the sample [25].

In Figure 6 (c), the micrograph of PLA with the addition of 2.0 wt% Carbon Nanotubes is presented. In this detailed analysis, the presence of pores (yellow arrows) and cracks (red arrows) distributed along the surface is identified. Additionally, clusters (orange arrows) are observed dispersed throughout the sample. It is noteworthy that, in micrograph 6 (c), the presence of MWCNTs-COOH is not discernible, which may be attributed to the quality of the polymer- nanofiller mixture [26].

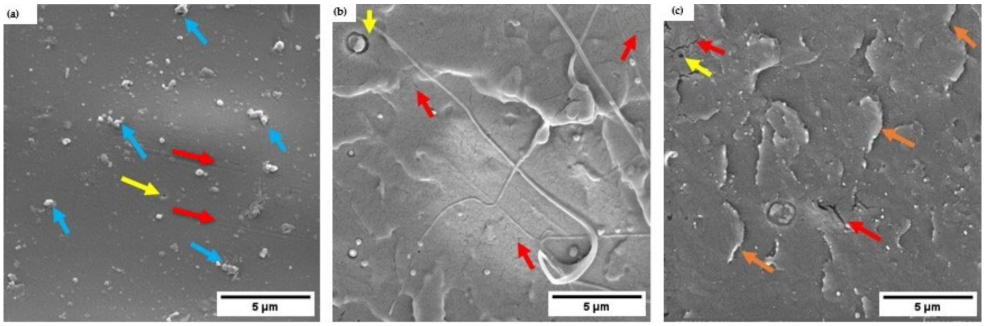

Figure 6. (a) SEM of PLA before the incorporation of CNTs, (b) SEM of PLA with the incorporation of 1.0 wt% CNTs, and (c) SEM of PLA with the incorporation of 2.0 wt% CNTs.

3.2. Characterization by X-ray Diffraction

The Carbon Nanotubes (CNTs), PLA, and nanocomposites (PLA/1.0%CNTs and PLA/2.0%CNTs) underwent characterization using X-ray Diffraction (XRD) technique, and the results are presented in the diffractogram of Figure 7.

The XRD results show that Carbon Nanotubes exhibited diffractions at 2θ: 30.01° and 2θ: 50.03°, attributed, according to [27], to the basal reflection peak and the graphitic crystalline lattice. As for PLA, both before and after 3D Printing, the results indicate the absence of crystallinity, revealing a slight curvature at 2θ: 8.2° and 2θ: 16.5°. Subsequently, the predominance of the amorphous phase of the polymer is observed, a behavior previously noted in studies by [24], [28], and [29]. Regarding the nanocomposites, PLA/1.0%CNTs and PLA/2.0%CNTs did not show significant changes in their respective crystallinities, exhibiting the disappearance of the curvature at 2θ: 8.2° and a slight curvature at 2θ: 18.7°. The disappearance at 2θ: 8.2°, as well as the disappearance of characteristic CNTs diffractions, can be attributed, according to [27], to the low dimensionality of MWCNTs clusters and their good dispersion in the matrix, resulting from the functionalization of carbon nanotubes.

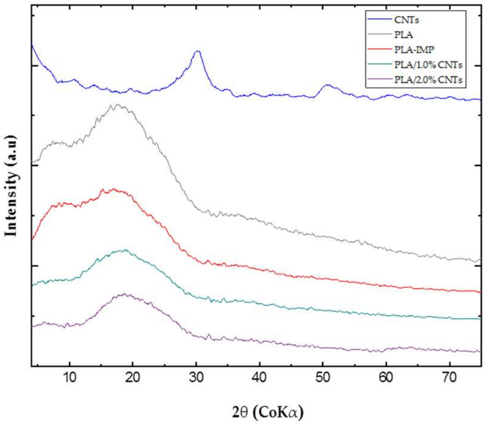

Figure 7. XRD of PLA, CNTs, and Nanocomposites.

3.3. Characterization by Raman Spectroscopy

Figure 8 presents the data obtained by Raman spectroscopy and treated by deconvolution into Lorentzian subbands for as-received carbon nanotube samples, the commercial PLA filament and the two nanocomposites produced respectively with 1.0 wt% and 2.0 wt% by mass of CNTs. The regions of interest were determined based on the main vibrational modes of the nanotubes, the first from 1200 to 1700 cm^{-1} and the second from 2600 to 3050 cm^{-1}.

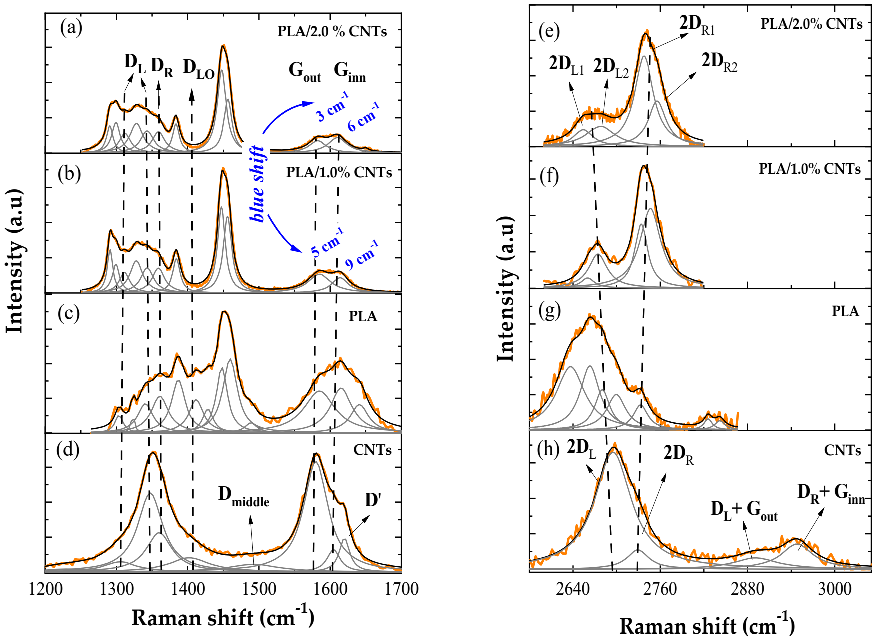

Figure 8. Deconvolution of the Raman spectra of the as-received carbon nanotube samples, the commercial PLA filament and the nanocomposites with 1.0 wt% and 2.0 wt% of CNTs.

As can be seen in Figures 8(a) and 8(b), the Raman spectra of the nanocomposites are a superposition of vibrational modes associated with the PLA polymer and the carbon nanotubes, shown in Figures 8(c) and 8(d). For the as-received CNTs, the D band was deconvoluted in three subbands, two labeled D_L and one labeled D_R, associated with defects and functionalizations on nanotubes walls related to sp^3 hybridized carbon, respectively in 1305, 1347 and 1360 cm^{-1} [24,30]. The subband D_{LO} in 1402 cm^{-1} is associated with longitudinal optic phonons in the CNTs structure and the subband D_{middle} in 1492 cm^{-1} has been used in literature as an indicator of the amorphous carbon degree on CNTs samples [30]. The G band was deconvoluted in three subbands, G_{out}, G_{inn} and D′ respectively in 1580, 1605 and 1620 cm^{-1}. The G_{out} and G_{inn} subbands are associated with the vibrations sp^2 hybridized carbon atoms of the outermost and the innermost walls of the carbon nanotubes, respectively, while the D′ subband is associated with structural disorder-induced double resonance process of the D band projected in the G band [24,30].

In this region, there are several vibrational modes for PLA, associated with stretching and bending vibrations of single and double-bonded carbon atoms and bonds between carbon and hydrogen, but the spectrum show some divergences with literature [24,31–33] such as vibrational modes in the same region of the G band of CNTs, these could be due to the production process of the commercial PLA. Even so, the most prominent band associated with CH_3 symmetric deformation vibrations was identified and deconvoluted with two subbands in 1448 and 1460 cm^{-1} and the the band associated with CH_3 asymmetric deformation vibrations was identified in 1387 cm^{-1} [31–33]. The spectra of the nanocomposites appeared as an overlap of these and the CNTs vibrational modes, as these same PLA modes were identified in 1447, 1456 and 1384 cm^{-1}. Furthermore, the signal from

PLA showed an enhancement as it is closer to the literature, which can be due the nanocomposites preparation methodology.

In both nanocomposite's spectra, the signal from PLA appeared with more intensity covering part of the signal from the CNTs. Although the D band isn't clearly visible, its subbands were identified in 1311, 1343 and 1359 cm^{-1}, but it is difficult to obtain information from these modes dislocations as they have low intensity and are in the same region of PLA modes. Similarly, the D_{LO}, D_{middle} and D' bands disappeared, but this can be due to the low signal intensity in comparison to the PLA spectrum. As a highlight, the G_{out} and G_{inn} subbands were identified respectively in 1585 and 1614 cm^{-1} for PLA/1.0%CNTs and in 1583 and 1610 cm^{-1} for PLA/2.0%CNTs, showing significant blueshift as shown in Figures 8 (a) and 8 (b). This indicates that the nanotubes are being compressed by the polymeric matrix, as they are distributed by its volume, which also could explain the lower signal of the CNTs. As they are randomly distributed, they could be subjected to different compressions and the region analyzed explains the higher blueshift in the sample with 1.0 wt% by mass of CNTs.

In Figures from 8 (e) to 8 (h) are shown the spectra in higher frequencies of the nanocomposites with 2. 0 wt% and 1.0 wt% by mass of CNTs, the commercial PLA and the as-received CNTs, respectively. The PLA spectrum also diverged from literature as shouldn't exist vibrational modes in this region [24,31–33], on the other hand the second order vibrational modes of CNTs were identified, as de 2D band was deconvoluted in $2D_L$ and $2D_R$ subbands and the D+G band in D_L+G_{out} and D_R+G_{inn} subbands, respectively in 2695, 2729, 2891 and 2948 cm^{-1} [34–36]. For the nanocomposites, the D+G band wasn't identified and the resulting spectra are attributed to the 2D band of the CNTs considering a split of both subbands, the redshift $2D_L$ and the blueshift $2D_R$ that resulted in the split of the 2D band itself. The $2D_L$ and $2D_R$ subbands are attributed to second order Raman scattering of the innermost and of the outermost tubes, respectively. For PLA/1.0%CNTs, the $2D_{L1}$ and the $2D_{L2}$ subbands were identified in 2660 and 2674 cm^{-1}, while for PLA/2.0%CNTs these subbands appeared in 2654 and 2678 cm^{-1}. Similarly, the $2D_{R1}$ and the $2D_{R2}$ subbands were identified in 2734 cm^{-1} and 2747 cm^{-1} for PLA/1.0%CNTs and in 2738 cm^{-1} and 2756 cm^{-1} for PLA/2.0%CNTs. For the $2D_R$ subbands the blueshift could indicate p-type doping of the outermost tubes and for the $2D_L$ subbands the redshift could indicate n-type doping of the innermost tubes. These results suggest that the doping effect can be due to the interaction between the CNTs and the polymeric matrix [34–36].

3.4. Compression Testing: Shape Solid Sample Variations of Infill Patterns

The strength of solid 3D-printed PLA samples with variable infill patterns (concentric, hexagonal, and triangular) and same percentages of 90%, was analyzed by means of mechanical compression tests. The results are presented in the following Table 1.

Table 1. Average compressive strength behavior of printed parts with different infill patterns.

Types of Samples/Infill Patterns	Filling Percentage	Compressive Strength (MPa)
PLA/Concentric	90 %	45.9 ± 6,5
PLA/Hexagon	90 %	48.5 ± 6,6
PLA/Triangle	90 %	52.8 ± 4,2

The results of the compression test show that there is a variation in the strength of the printed parts as the infill pattern changes. According to the results, it can be observed that the solid sample with a triangle infill pattern exhibits a higher average compression strength, followed by the hexagonal infill pattern. In addition, it is possible to observe that the infill pattern that presented the lowest mechanical performance was the concentric pattern.This behavior has already been observed in the study conducted by [37] when investigating PLA printed parts with varying infill patterns. In their research, they achieved better compression performance for samples with a triangular infill pattern compared to line type infill. [38] emphasize that the compressive properties of 3D-printed materials (such as PLA) depend on the infill patterns and infill percentages; these factors influence the mechanical properties of the parts.

Figure 9 (a) illustrates the comparisons of solid materials (patterns: triangular, hexagonal, and concentric) regarding their compression strengths. Upon analyzing the figure, it can be observed that the printed material exhibiting the highest average compression strength was the PLA sample with a triangular infill pattern, with an increase of 15.03% compared to the concentric, and 8.8% compared to the hexagonal. And, Figure 9 (b) shows the percentage Stress x Strain behavior of the PLA with different infill patterns under mechanical compression loading.

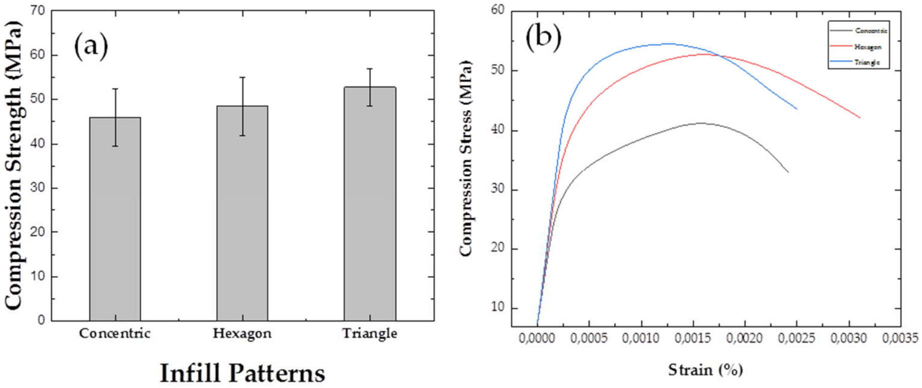

Figure 9. (a) Comparative analysis of compressive strength of 3D printed PLA samples with variations infill patterns and 9 (b) Deformation of the PLA with different infill patterns when subjected to mechanical analysis of compression.

3.5. Compression Test: Nanocomposites PLA with 1.0 wt% and 2.0 wt% CNTs

The evaluation of the mechanical strength of the nanocomposites of PLA and CNTs was conducted by performing compression tests, and the corresponding results are presented in Table 2.

Table 2. Average Compression Strength Behavior of Nanocomposites.

Types of Samples/Infill Patterns	Filling Percentage	Compressive Strength (MPa)
PLA/Triangles	90 %	52.8 ± 4,2
PLA/1.0%CNTs/ Triangles	90%	61.7 ± 12,1
PLA/2.0%CNTs/Triangles	90%	73.5 ± 15,0

The results demonstrate that the addition of Carbon Nanotubes to the matrix enhances the compression strength of the nanocomposites. There is a noticeable 20.32% increase in compression strength for the nanocomposite containing 2.0 wt% CNTs compared to the nanocomposite with 1.0 wt% CNTs in its composition. All nanocomposites exhibited higher strength than the matrix with a triangular infill pattern.

The nanocomposite with 1.0 wt% of CNTs in its composition shows an increase in compression mechanical strength of 16.8% compared to the matrix. Furthermore, for the nanocomposite with 2.0 wt%, the increase is even more significant, reaching 39.2% compared to the matrix.

Contrary to what was observed in the study conducted by [39], where the analysis of the influence of graphene in the PLA matrix didn't result in an increase in compression strengths compared to the PLA matrix, this work reveals a significant contribution of carbon nanotubes (CNTs) to the mechanical compression performance. It is noteworthy that, to date, there are no records in the literature regarding PLA/CNTs nanocomposites under the specific conditions evaluated in this study.

The results regarding average compression strength are visualized in Figure 10 (a), which illustrates the comparison between the matrix (configured with a triangular infill pattern) and the

doi:10.20944/preprints202402.0299.v1

nanocomposites (PLA/1.0%CNTs and PLA/2.0%CNTs). In the figure, it is evident that the nanocomposites show significantly higher compression strengths when contrasted with the matrix. And 10 (b) graphically depicts the Stress-Strain behavior of PLA polymer and PLA/CNTs nanocomposites at concentrations of 1.0 wt% and 2.0 wt%, respectively.

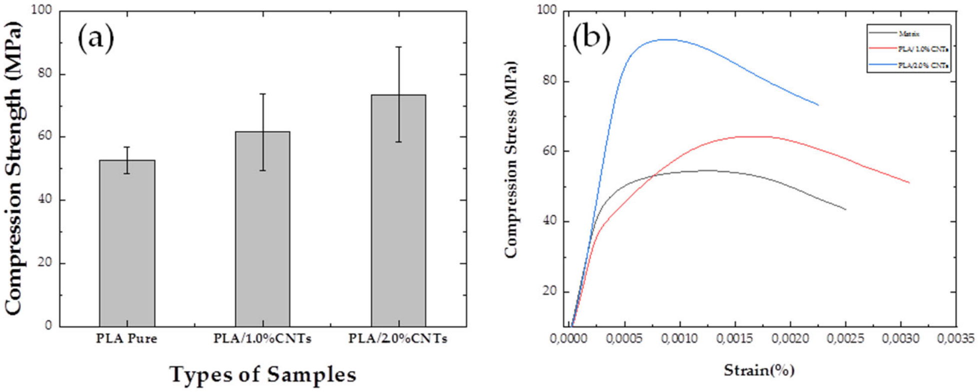

Figure 10. (a) Comparative Analysis of Compression Strength between PLA Matrix and PLA/CNTs Nanocomposites and (b) Stress-Strain Behavior of PLA and Nanocomposites under Compression Analysis.

3.6. Compression Testing: Honeycomb Shape with Variations of Infill Patterns

In the mechanical compression analysis, honeycomb structures with variations in infill patterns (concentric, hexagonal, and triangular) exhibited behaviors similar to the structures analyzed by [40] and [41]. Where, in their studies presented three distinct regions: Elastic, Plateau and densification.

According by [42], the three regions of the stress-strain graph are associated with three different failure modes at each stage of compaction. Initially, the material is subjected to elastic bending, represented by the almost linear portion until the maximum crushing force. This is followed by elastic buckling and subsequent densification of cells during the final stages of loading.

However, in the scope of this study, we will delimit our analysis to compressive properties restricted to the elastic region. Thus, in the subsequent table, the results of the compression test of the honeycomb samples are presented, considering variations in the infill patterns (concentric, hexagonal and triangular).

Table 3. Average Compression Strength Behavior of Printed Parts with Different Infill Patterns.

Type of Samples/Infill Patterns	Filling Percentage	Compressive Strength (MPa)
Honeycomb/Concentric	90 %	20.6 ± 1,9
Honeycomb/Hexagon	90 %	19.6 ± 4,6
Honeycomb/Triangles	90 %	20.8 ± 2,2

The results obtained from the compression test of honeycomb samples, considering variations in infill patterns (concentric, hexagonal, and triangular), demonstrate that the structures exhibit remarkably equivalent compression strength. It is noteworthy, however, that the Honeycomb/Triangles configuration exhibits superior compressive performance compared to the other analyzed forms.

Figures 11 (a) and 11 (b) illustrate, respectively, the average compression strength and the stress-strain behavior of honeycomb-printed structures with variations in infill patterns.

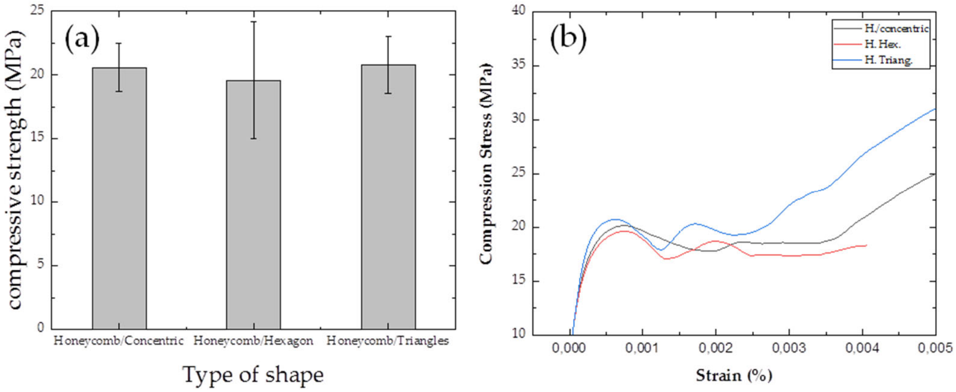

Figure 11. (a) Comparative analysis of compression strength in honeycomb samples with different infill patterns and (b) Stress-Strain Behavior of honeycomb shape with different infill patterns.

3.7. Compression Test: Honeycomb Samples with 1.0 wt% and 2.0 wt% Carbon Nanotubes

The results of the compression test for nanostructured honeycomb samples, containing carbon nanotubes (CNTs) at concentrations of 1.0 wt% and 2.0 wt%, and the matrix (triangular infill pattern), are presented in the table below.

Table 4. Average Compression Strength of the Matrix and Nanocomposites.

Type of samples/Infill Patterns	Filling Percentage	Compressive Strength (MPa)
Honeycomb/Triangles	90 %	20.8 ± 2,2
Honeycomb/1.0%CNTs	90 %	33.2 ± 2,2
Honeycomb/2.0%CNTs	90 %	20.9 ± 4,4

The results show a 59.6% increase in compressive strength for the nanocomposite sample (PLA/1.0%CNTs) compared to the sample without addition of CNTs. As for the nanocomposite sample (PLA/2.0%CNTs), the increase is 0.48%. However, contrary to what occurs in solid samples, where an increase in mean compressive resistance is observed with the increase in the percentage of CNTs in the matrix, there is reduction in resistance as the percentage of CNTs in the matrix increases.

It is noteworthy that, up to the present moment, there are no reports in the literature regarding investigative studies of nanostructured honeycomb structures PLA/CNTs under the specific conditions examined in this research.

Figures 12 (a) and 12 (b) represent, sequentially, the average compressive strength and stress-strain behavior of the structures printed in the honeycomb configuration, showing variations in percentages of CNTs.

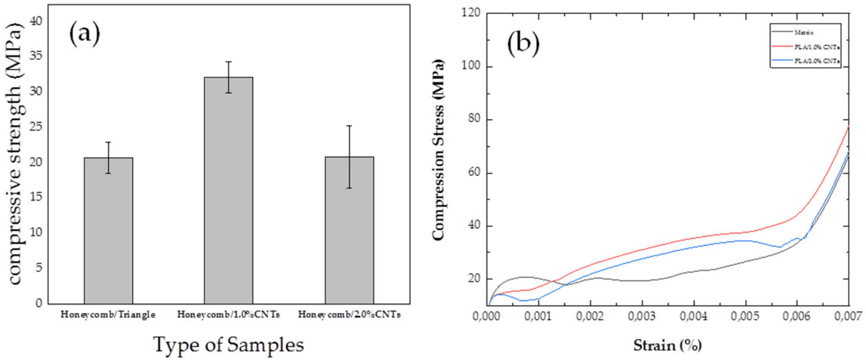

Figure 12. (a) Comparative analysis of compression strength in honeycomb samples with variations in percentages of CNTs and (b) Stress-Strain Behavior of the matrix and nanostructured honeycomb.

doi:10.20944/preprints202402.0299.v1

3.8. Morphological Analysis via SEM After the Compression Test

The solid and honeycomb shaped PLA samples containing variations in infill patterns were subjected to Scanning Electron Microscopy (SEM) analysis, and the results obtained are illustrated in the figures below:

The results of the Scanning Electron Microscopy analysis shown in Figure 13 reveal in (a) micrographs corresponding to the solid sample with a concentric infill pattern, highlighting highly compacted regions (blue arrows) that can be attributed to deformations resulting from the mechanical test. Additionally, the presence of folds in the structure is observed (yellow arrow), which could be associated with both the manufacturing process and the responses of the mechanical analysis.

In Figure 13 (b), the micrograph of the honeycomb shape structure is presented, showing the presence of voids throughout the structure, which can be associated with the internally distributed honeycomb configuration.

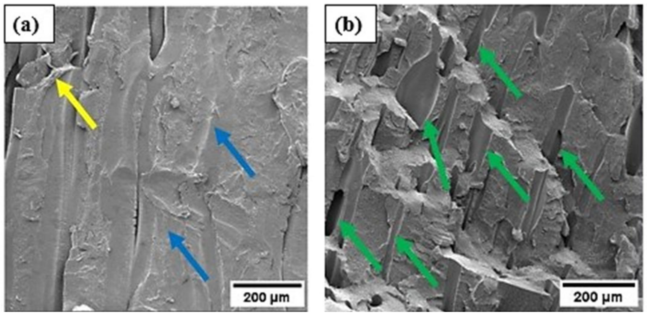

Figure 13. (a) Micrograph of the solid shape and (b) honeycomb with a concentric infill pattern.

In Figure 14, micrographs corresponding to the solid test specimen with a hexagon infill patterns are displayed in (a), and those of the honeycomb shaped structure with the same infill pattern are shown in (b).

In 14 (a), the occurrence of structure ruptures is observed (yellow arrows), which can be attributed, as mentioned earlier, to the mechanical loading. Additionally, compacted structures are observed (red arrows), mechanisms already noted in the micrograph with concentric infill patterns.

In 14 (b), the micrograph of the honeycomb-shaped structure with hexagonal infill patterns is shown. Here, mechanisms such as structure folds (black arrows), layer stacking (orange arrows), and the presence of voids (blue arrows) are observed. The voids can be attributed to the arrangements of the hexagons within the structures.

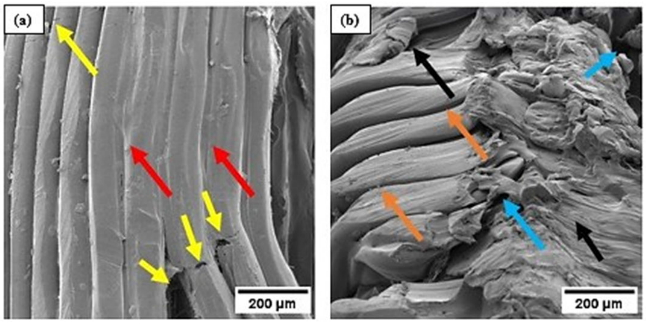

Figure 14. (a) Micrograph of the solid shape, and (b) honeycomb with hexagonal infill pattern.

Figure 15 displays micrographs corresponding to the shape solid (a) and the honeycomb (b) with triangle infill patterns.

In the micrograph of the solid test specimen with triangle infill patterns, as presented in 15 (a), the presence of compacted structures is noticeable (orange arrows), a mechanism observed in other solid structures analyzed in this study. Additionally, fractures in the structure are observed (blue arrows), which can be attributed to increased load during the mechanical analysis, leading to structural ruptures.

In Figure 15 (b), the micrograph of the honeycomb-shaped structure with triangle infill patterns is illustrated. Here, well-compacted structures are noted (red arrows), and the presence of voids (yellow arrows) is observed again, associated with the honeycomb-like configuration of the structure.

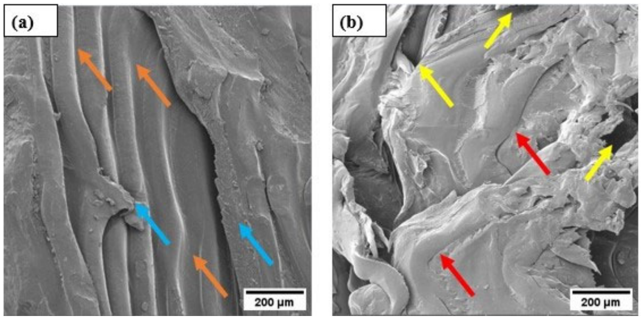

Figure 15. a) Micrograph of the solid shape, and (b) honeycomb shaped structure with triangular infill pattern.

The nanocomposite solid (PLA/1.0%CNTs) and (PLA/2.0%CNTs), subjected to the mechanical compression test, were microscopically analyzed by SEM, with the results presented in Figure 16.

In 16 (a), layer rupture is observed (green arrow), which can be attributed to mechanical stresses during the compression test; additionally, the layers can be seen compacting onto each other (orange arrows). In 16 (b), voids (black arrows) in the structure are observed, along with cracks (red arrows) and detachment (white arrows). The mechanisms present in the fractures of the nanocomposites are similar to those exhibited in PLA samples without the addition of Carbon Nanotubes.

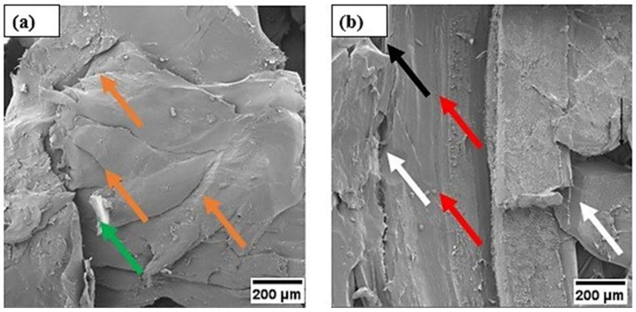

Figure 16. Micrograph of the nanocomposite (PLA/1.0%CNTs) in (a) and (b) PLA/2.0%CNTs.

Figure 17 (a) illustrates the micrograph of the honeycomb nanostructure (PLA/1.0%CNTs) and (PLA/2.0%CNTs).

In micrograph (a), the presence of detachment (red arrows) and cracks (white arrows) is highlighted. In micrograph 17 (b), there is a widespread presence of cracks (white arrows) throughout the structure, along with compacted areas (black arrows). These deformations, including cracks and detachment, can be attributed to the applied forces during the mechanical compression analysis.

doi:10.20944/preprints202402.0299.v1

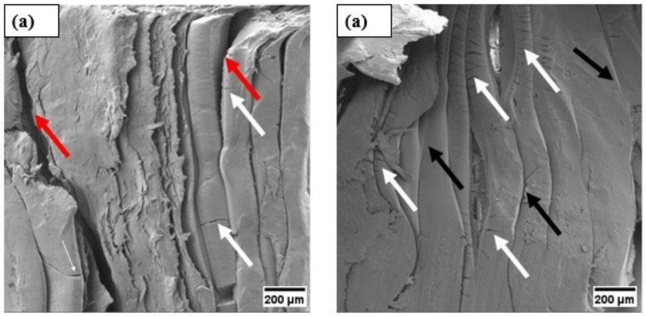

Figure 17. a) Micrograph of the nanostructured honeycomb shape (PLA/1.0%CNTs) and (b) Nanostructured honeycomb shape (PLA/2.0%CNTs).

4. Conclusions

In this study, the analyzed materials were characterized using: SEM, X-ray Diffraction, Raman Spectroscopy, and compression testing. The obtained results reveal the following conclusions:

a) The SEM characterization of PLA filaments before and after the incorporation of Carbon Nanotubes reveals the presence of clusters, pores, CNTs and cracks.

b) X-ray Diffraction analysis of CNTs, PLA, and nanocomposites (PLA/1.0%CNTs and PLA/2.0%CNTs) provided insights into their crystallographic properties. CNTs exhibited characteristic diffractions, while PLA, both before and after 3D Printing, showed an absence of crystallinity, indicating a predominance of the amorphous phase. The nanocomposites PLA/1.0%CNTs and PLA/2.0%CNTs demonstrated minimal changes attributed to functionalization and the low dimensionality of MWCNTs clusters.

c) In Raman analysis, the CNTs had their bands (D and G) deconvoluted into three sub-bands. The PLA exhibited its respective vibrational modes associated with stretching and bending of carbon atoms, symmetric and asymmetric deformation vibrations of CH_3. The vibrational modes of the nanocomposites are an overlap of the vibrational modes of both CNTs and PLA.

d) In the mechanical analysis of compression, the triangle pattern outperforms others with a 15.03% increase over concentric and 8.8% over hexagonal. In solid nanocomposites, PLA/1.0%CNTs exhibits a 16.8% increase, while PLA/2.0%CNTs shows a 39.2% increase compared to the matrix. For the honeycomb shape, the triangular pattern excels, showing a 0.97% increase over concentric and 6.12% over hexagonal. The nanostructured honeycomb PLA/1.0%CNTs surpasses the matrix by 59.6%, reaching and honeycomb PLA/2.0%CNTs has a 0.48% increase, reaching.

e) A SEM analysis conducted after the mechanical compression test illustrates the mechanisms present in the material, such as detachment of structures, presence of compacted regions, internal voids, rupture, and cracks, which can be attributed to the application of stress.

f) In this study, the direct influence of infill patterns and the percentages of CNTs on compressive mechanical properties is observed. Therefore, when employing the Fused Deposition Modeling (FDM) technique in the development of new materials, it becomes essential to investigate these parameters to achieve enhanced performances tailored to different applications.

Author Contributions: Conceptualization, R.A., S.P. and M.R.; methodology, R.A., S.P., M.R. and D.F.; software, D.O. and L.Q.; validation, D.F. and M.R.; formal analysis, S.P. and M.R.; investigation, M.S., M.P., D.F. and M.R.; writing—original draft preparation, L.Q., D.F. and M.R.; writing—review and editing, D.F., L.Q. and M.R. All authors have read and agreed to the published version of the manuscript.

Funding: This research was funded by FINEP, n_ 01.22.0133.00.

Institutional Review Board Statement: Not applicable.

Data Availability Statement: Not applicable.

Acknowledgments: The authors thank CAPES and PROPESP/UFPA (PAPQ) for their support during this research. D.F and M.R. thank the LABNANO-AMAZON/UFPA network for supporting Raman and SEM. Soli Deo Gloria.

Conflicts of Interest: The authors declare no conflict of interest.

References

1. ASTM D695-15. Standard Test Method for Compressive Properties of Rigid Plastics. ASTM International, 2015.
2. AWASTHI, P.; BANERJEE, S. S. Fused deposition modeling of thermoplastic elastomeric materials: Challenges and opportunities. *Additive Manufacturing*, **2021**, *Volume* 46, p. 102177.
3. LIU, G. *et al*. Additive manufacturing of structural materials. *Mater. Sci. Eng., R*, **2021**, *Volume* 145, p. 100596.
4. ÁDÁM, B.; WELTSCH, Z. Thermal and Mechanical Assessment of PLA-SEBS and PLA-SEBS-CNT Biopolymer Blends for 3D Printing. *Appl. Sci.*, **2021**, *Volume* 11, n. 13, p. 6218.
5. MWEMA, F. M. *et al*. Basics of fused deposition modelling (FDM). *Fused deposition modeling: strategies for quality enhancement*, **2020**, p. 1-15.
6. WICKRAMASINGHE, S.; DO, T.; TRAN, P. FDM-based 3D printing of polymer and associated composite: A review on mechanical properties, defects and treatments. *Polymers*, **2020**, *Volume* 12, n. 7, p. 1529.
7. SYRLYBAYEV, D. *et al*. Optimisation of strength properties of FDM printed parts—A critical review. *Polymers*, **2021**, *Volume* 13, n. 10, p. 1587.
8. SIRIPONGPREDA, T. *et al*. Emerging 3D printing based on polymers and nanomaterial additives: Enhancement of properties and potential applications. *European Polymer Journal*, **2023,** *Volume* 184, p. 111806.
9. LOPEZ DE ARMENTIA, S. *et al*. Advances in biodegradable 3D printed scaffolds with carbon-based nanomaterials for bone regeneration. *Materials*, **2020**, *Volume* 13, n. 22, p. 5083.
10. OMANOVIĆ, E. O. *et al.* Nanocomposites: a brief review. *Health and Technology*, **2020**, *Volume* 10, n. 1, pág. 51-59.
11. SHAMEEM, M.M. *et al.* A brief review on polymer nanocomposites and its applications. *Mater. Today Proc*, **2021**, *Volume* 45, p.2536-2539.
12. BOROUMAND, F.; SEYEDKASHI, SM H.; POL, M. H. Experimental study of mechanical properties and failure mechanisms of metal–composite laminates reinforced with multi-walled carbon nanotubes. *Thin-Walled Structures***, 2023**, *Volume* 183, p. 110377.
13. SMAIL, A. H. M. *et al.* On the enhancement of the fatigue fracture performance of Polymer matrix composites by reinforcement with carbon nanotubes: a systematic review. *Carbon Letters*, **2022**, *Volume* 32, n. 3, pág. 727-740.
14. KHODAKARAMI, M., BAGHERI, M. Recent advances in synthesis and application of polymer nanocomposites for water and wastewater treatment, *Journal of Cleaner Production*, **2021**, *Volume* 296, p. 126404.
15. AL RASHID, A. *et al*. Additive manufacturing of polymer nanocomposites: Needs and challenges in materials, processes, and applications. *J. Mater. Res. Technol.,* **2021**, *Volume* 14, p. 910-941.
16. IBRAHIM, A. *et al*. Graphene-Based Nanocomposites: Synthesis, Mechanical Properties, and Characterizations. *Polymers*, **2021**, *Volume* 13, n. 17, p. 2869.
17. ATES, M.; EKER, A. A; EKER, B. Carbon nanotube-based nanocomposites and their applications. *Journal of adhesion science and Technology*, **2017**, *Volume* 31, n. 18, p. 1977-1997.
18. DE BORTOLI, L. S. *et al*. Functionalized carbon nanotubes for 3D-printed PLA-nanocomposites: Effects on thermal and mechanical properties. *Materials Today Communications*, **2022**, *Volume,* 31, p. 103402.
19. MOHD NURAZZI, N. *et al.* fabrication, functionalization, and application of carbon nanotube-reinforced polymer composite: an overview. *Polymers*, **2021**, *Volume* 13, n. 7, p. 1047.
20. YANG, H. *et al*. Preparation of hydrophobic surface on PLA and ABS by fused deposition modeling. *Polymers*, **2020,** *Volume* 12, n. 7, p. 1539.
21. JEM, K. J.; TAN, B. The development and challenges of poly (lactic acid) and poly (glycolic acid). *Advanced Industrial and Engineering Polymer Research*, **2020**, *Volume* 3, n.2, p. 60-70.
22. SINGH, J.; GOYAL, K. K.; KUMAR, R. Effect of filling percentage and raster style on tensile behavior of FDM produced PLA parts at different build orientation. *Mater. Today Proc.,* **2022**, *Volume* 63, p. 433-439.
23. SOLTANI, A. *et al*. 3D printing on-water sports boards with bio-inspired core designs. *Polymers*, **2020**, *Volume* 12, n. 1, p. 250.
24. ZHOU, X. *et al*. Additive manufacturing of CNTs/PLA composites and the correlation between microstructure and functional properties. *J. Mater. Sci. Technol.,***2021**, *Volume* 60, p. 27-34.
25. KARTIKEYAN, B. *et al*. Experimental and theoretical analysis of FDM AM PLA mechanical properties. *Mater. Today: Proceedings*, **2023**.
26. PINTO, V.C. et al. Dispersion and failure analysis of PLA, PLA/GNP and PLA/CNT-COOH biodegradable nanocomposites by SEM and DIC inspection. *Engineering Failure Analysis*, **2017,** *Volume 71*, p. 63-71.
27. KOTSILKOVA, R *et al*. Essential nanostructure parameters to govern reinforcement and functionality of poly (lactic) acid nanocomposites with graphene and carbon nanotubes for 3D printing application. *Polymers*, **2020,** *Volume* 12, n. 6, p. 1208.

28. TERZOPOULOU, Z. *et al*. Interfacial interactions, crystallization and molecular mobility in nanocomposites of Poly (lactic acid) filled with new hybrid inclusions based on graphene oxide and silica nanoparticles. *Polymer*, **2019**, *Volume* 166, p. 1-12.
29. CAO, M. *et al*. Investigation of Carbon Fiber on the Tensile Property of FDM-Produced PLA Specimen. *Polymers*, **2022**, *Volume* 14, n. 23, p. 5230.
30. DOS REIS, M. A. L. *et al*. Raman spectroscopy fingerprint of stainless steel-MWCNTs nanocomposite processed by ball-milling. *AIP Advances*, **2018,** *Volume* 8, n. 1.
31. CUIFFO, M. A. *et al*. Impact of the fused deposition (FDM) printing process on polylactic acid (PLA) chemistry and structure. *Applied Sciences*, **2017**, *Volume* 7, n. 6, p. 579.
32. SUZUKI, T. *et al*. Application and analysis of a DSC-Raman spectroscopy for indium and poly (lactic acid). *Journal of thermal analysis and calorimetry*, **2013**, *Volume* 113, p. 1543-1549.
33. KISTER, G.; CASSANAS, G.; VERT, M. Effects of morphology, conformation and configuration on the IR and Raman spectra of various poly (lactic acid) s. *Polymer*, **1998,** *Volume* 39, n. 2, p. 267-273.
34. BATAKLIEV, T. *et al.* Physico-chemical characterization of PLA-based composites holding carbon nanofillers. *Applied Composite Materials*, **2021**, *Volume* 28, n. 4, p. 1175-1192.
35. SAITO, R. *et al*. Raman spectroscopy of graphene and carbon nanotubes. *Advances in Physics*, **2011,** *Volume* 60, n. 3, p. 413-550.
36. REBELO, S. L.H. *et al*. Progress in the Raman spectra analysis of covalently functionalized multiwalled carbon nanotubes: unraveling disorder in graphitic materials. *Physical Chemistry Chemical Physics*, **2016,** *Volume* 18, n. 18, p. 12784-12796.
37. PARAB, S.; ZAVERI, N. Investigating the influence of infill pattern on the compressive strength of fused deposition modelled PLA parts. *In: Proceedings of International Conference on Intelligent Manufacturing and Automation: ICIMA*. Springer Singapore, **2020**, p. 239-247.
38. SUBESHAN, B. et al. Investigating compression strengths of 3D printed polymeric infill specimens of various geometries. *In: Nano-, Bio-, Info-Tech Sensors, and 3D Systems II. SPIE*, **2018**. p. 89-94.
39. VIDAKIS, N. et al. A comprehensive investigation of the mechanical behavior and the dielectrics of pure polylactic acid (PLA) and PLA with graphene (GnP) in fused deposition modeling (FDM). *International Journal of Plastics Technology*, **2019**, *Volume* 23, n. 2, p. 195-206.
40. AUSTERMANN, J. *et al*. Fiber-reinforced composite sandwich structures by co-curing with additive manufactured epoxy lattices, *J. compos. sci*., **2019** *Volume* 3, n. 2, p. 53.
41. SALEH, M. *et al.* Compression performance and failure analysis of 3D-printed carbon fiber/PLA composite TPMS lattice structures. *Polymers*, **2022** *Volume* 14, n. 21, p. 4595.
42. JOSEPH: A.; MAHESH, V.; MAHESH, V. Effect of loading rates on the in-plane compressive properties of additively manufactured ABS and PLA-based hexagonal honeycomb structures. *J. Thermoplast. Compos. Mater*., **2023,** *Volume* 36, n. 3, p. 1113-1134.